Two-dimensional electron density visualization over plasma flare in vacuum breakdown process

Y. Inada,[a] T. Kamiya, S. Matsuoka, A. Kumada, H. Ikeda, and K. Hidaka
Department of Electrical Engineering and Information Systems, The University of Tokyo, 7-3-1 Hongo Bunkyo-ku, Tokyo 113-8656, Japan

Spatiotemporal evolution of plasma flares in a vacuum breakdown process was characterized by various optical techniques including Shack-Hartmann type laser wavefront sensors for two-dimensional electron density imaging, high-speed framing photography for speed determination of flare expansion, and optical emission spectroscopy for plasma composition assessment. The experimental results showed that the plasma flares with high electron densities of 10^{25} m^{-3} and gas temperature of 2 eV were initiated on the copper anode and expanded to the vacuum gap with a propagation speed of 6×10^3 m/s. Subsequently, the electron densities in the anode flare tips demonstrated a drastic decrease in a short time scale of 50 ns due to a three-body recombination reaction. The anode flare tips combined with the cathode plasma flares initiated on the copper cathode, and the conductive plasma channels containing flare-induced copper vapor were established in the interelectrode gap. In the final stage of the vacuum breakdown, the copper-vapor-contaminating plasmas were deconstructed and they transformed into the vacuum arc discharges. *Published by AIP Publishing.* https://doi.org/10.1063/1.5035100

I. INTRODUCTION

Spark conditioning is widely used for the improvement of dielectric strength of vacuum circuit breakers.[1,2] The optimization of the spark conditioning requires a fundamental knowledge on the physical mechanism of vacuum breakdown phenomena,[3,4] which are initiated by plasma flares. In addition to the spark conditioning, there has been an increasing interest in actively utilizing the plasma flares as a source of the high-intensity extreme ultraviolet radiation source for further development and optimization of semiconductor lithographic technology.[5–9] In order to realize the remarkable advances in the modern industry by using the plasma-flare-related technology, the complete modeling and precise controlling of plasma flares are crucially important, which are achieved by the detailed observation of the spatiotemporal evolution of the plasma flares.

Historically, the experimental observation of the plasma flare behavior has been an extremely active area of research with an early report on photography using a high speed rotating mirror described by Chiles in 1937.[10] A large number of researchers have been studying the expansion speed of the plasma flares for elucidating switching mechanisms in vacuum tubes.[11–13] Qualitative composition of plasma flares was studied by using the spectroscopic method.[14] Differential dye laser absorption photography was conducted for the visualization of the plasma flares with a high spatiotemporal resolution of a micrometer-nanosecond scale.[15] Here, one of the important fundamental physical quantities for understanding the plasma flare behavior is electron density. Although a few electron density measurements have been conducted by the interferometric method,[16] Stark broadening,[5,6,9] and Thomson scattering,[5,6,9] the visualization of the spatiotemporal electron density evolution over every stage ranging from the plasma flare generation to the extinction has never been achieved. Furthermore, the physical mechanism of the spatiotemporal electron density evolution has never been understood for the plasma flares.

Recently, Shack-Hartmann type laser wavefront sensors have been developed as novel means of single-shot visualization of two-dimensional electron density distributions over discharge plasmas.[17–19] In spite of the recent advances of this technique, the Shack-Hartmann sensors have never been applied to the breakdown processes in vacuum. In this paper, we describe the systematic characterization of the plasma flares generated between copper electrodes. Such comprehensive characterization was achieved by using various optical techniques including 50-ns time-resolved Shack-Hartmann sensors for two-dimensional electron density imaging, high-speed framing photography for propagating speed determination, and optical emission spectroscopy for plasma composition assessment. A combination of these experimental data is used for the discussion on an electron consumption mechanism and estimation of the gas temperature and pressure in the plasma flares.

II. EXPERIMENT

A. Electrical circuit

The electrical circuit for generating plasma flares is illustrated in Fig. 1. A 0.6-μF capacitor was charged up to 32 kV through a 100-kΩ resistor. The 32 kV was higher than the charging voltage causing the vacuum breakdown in the present setup by 2 kV. After the capacitor charging was completed, by turning the mechanical switch on, the plasma flares were generated in a 3-mm vacuum gap. The vacuum
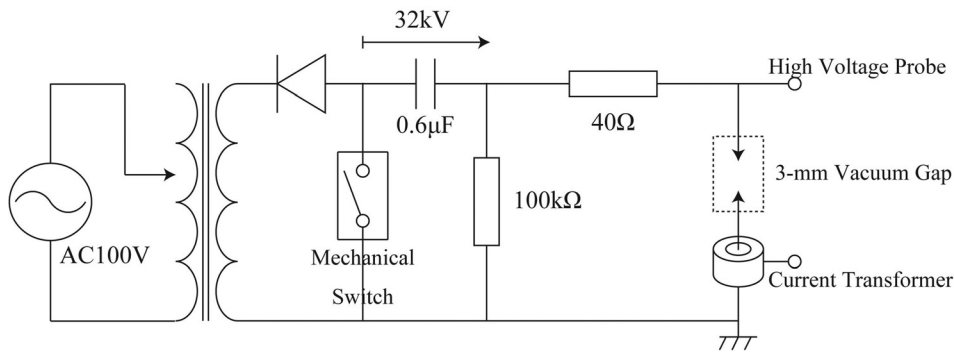
a)Electronic mail: inada@p-front.t.u-tokyo.ac.jp

FIG. 1. Electrical circuit for generating plasma flare.

gap was composed of rod-to-rod copper electrodes of 1 mm in diameter, as shown in Fig. 2. The rod electrodes were cut out of a copper plate by a copper-wire cutter, polished by paper and finished by ultrasonic water cleaning. The vacuum gap was installed in a 0.2-m-diameter stainless-steel vacuum vessel evacuated to an ambient pressure of 10^{-4} Pa. Figure 3(a) shows the typical voltage and current waveforms for the vacuum breakdown. The accompanying error ranges demonstrates the shot-to-shot variations of the voltage and current waveforms, which were ± 3 kV and ± 15 A, respectively. The applied voltage on the anode V (V) was measured by a high voltage probe connected to the center conductor of the insulation cylinder on the top of vacuum vessel. The probe connection point was located at the outside of the insulation cylinder. The voltage waveform was not corrected for inductive voltage drop over the center conductor of the insulation cylinder. The second maximum in the voltage waveform was mainly caused by the resonance oscillation due to the residual inductance and parasitic capacitance of the high voltage cable. The measurement of the electrical current I (A) was conducted by using a current transformer. Figure 3(b) shows the case where the displacement current was eliminated from the electrical current depicted in Fig. 3(a). As described later,

framing photography demonstrated protrusion explosion on the cathode prior to the generation of the plasma flares. The time of the explosion occurrence was defined as $t = 0$ ns in this study. After the plasma flare extinction, sustained vacuum arcs were established and the arc current flowed through a current limiting resistance of 40 Ω. The peak value and damping time constant of the arc current were 710 A and 24 μs, respectively. The peak current density was $\sim$500 A/mm^2, which caused the intense-mode vacuum arcs[19] usually observed in the high current interruption.

B. Shack-Hartmann type laser wavefront sensor

A detailed description of an electron density measurement using Shack-Hartmann type laser wavefront sensors was previously reported.[20] Our electron density measuring sensors visualize two-dimensional wavefront gradient profiles over the cross-sectional areas of expanded laser beams transmitted through discharge plasmas. Since the wavefront gradients of the laser light are expressed as a function of electron densities in discharge plasma, a two-dimensional electron density image is obtained from only a single recording. Figure 4 shows the basic concept of a Shack-Hartmann sensor for measuring electron density distribution in discharge plasma. A Shack-Harmann sensor is composed of an image camera and microlens arrays. The localized wavefront gradients of a laser beam are converted into shifts of the focal spot positions.[21,22] These spot shifts are observed using the image camera at any given time after plasma generation. The moving distances of the focal spots $T(\lambda)$ (m) for laser wavelength λ (m) are determined by the number densities of neutral particles, positive ions, and electrons in the plasma. In particular, only the contribution from electrons to $T(\lambda)$ depends on λ, whereas the contribution from neutral particles and positive ions is independent of λ. Therefore, our electron density sensing system requires a simultaneous measurement of $T(\lambda_1)$ and $T(\lambda_2)$ using two lasers with different wavelengths λ_1 and λ_2. The electron density is obtained from the value of $T(\lambda_1)$–$T(\lambda_2)$ with the elimination of the influence of other particle densities. The experimental and analytical procedures involve: (i) simultaneous spot shift measurements using two lasers with different wavelengths; (ii) calculation of line-integrated electron density profiles using the radial components of the spot shifts; (iii) approximation of the profiles by Gaussian functions; and (iv) inverse Abel transformation to the Gaussian functions for obtaining the electron
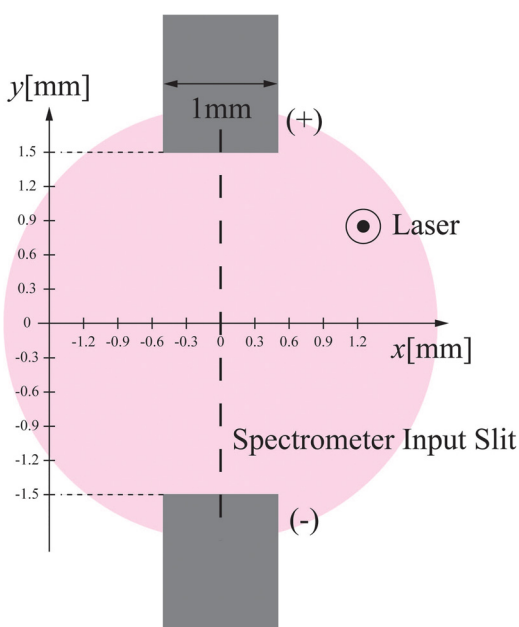

FIG. 2. 3-mm vacuum gap composed of rod-to-rod copper electrode of 1 mm in diameter.

(a) with displacement current   (b) without displacement current
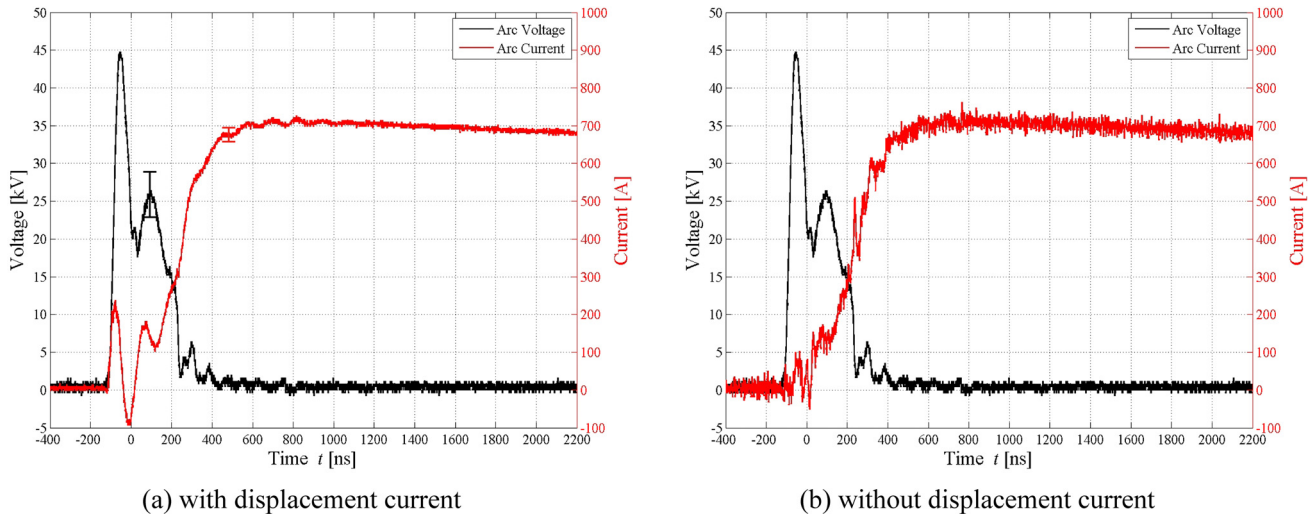
FIG. 3. Voltage and current waveform.

density profiles under the assumption of axial symmetry of the discharge plasma.

The aforementioned simultaneous two-wavelength measurement is required for the electron density imaging over weakly ionized plasmas including neutral particles. On the other hand, electron density visualization of fully ionized plasmas is achieved by using single-wavelength method because the ion contribution to $T(\lambda)$ is still smaller than that of electrons at the wavelengths used in this study[23] and as a result of this, the $T(\lambda)$ is mainly determined by only the electron densities. As discussed later in Subsection III B, the plasma flares were almost fully ionized in the time range of $100 \leq t \leq 250$ ns. Therefore, the single-wavelength method was applied to the electron density imaging over the almost fully ionized plasma flares in $100 \leq t \leq 250$ ns. The laser

wavelength for the single-wavelength method was 784 nm. Electron density measurements were conducted at $t = 100$, 150, 200, 250, 300, 350, 400, and 550 ns.

The electron density sensing system used in this study employed two continuous-wave diode lasers (TOPTICA PHOTONICS Inc. iBEAM-SMART-785-S; $\lambda_1 = 784$ nm, TOPTICA PHOTONICS Inc. iBEAM-SMART-405-S; $\lambda_2 = 408$ nm) capable of constantly producing relatively flat wavefronts, a sheet of microlens arrays (Nikon Corporation; pitch $P = 250\,\mu$m; focal length $f = 1$ mm; array number $= 50 \times 50$; $t = 100$, 150, 200, and 250 ns, Nikon Corporation; $P = 250\,\mu$m; $f = 20$ mm; array number $= 50 \times 50$; $t = 300$ and 350 ns, advanced microoptic systems gmbh; $P = 300\,\mu$m; $f = 467$ mm; array number $= 40 \times 40$; $t = 400$ and 550 ns), and an ICCD (intensified charge-coupled device)
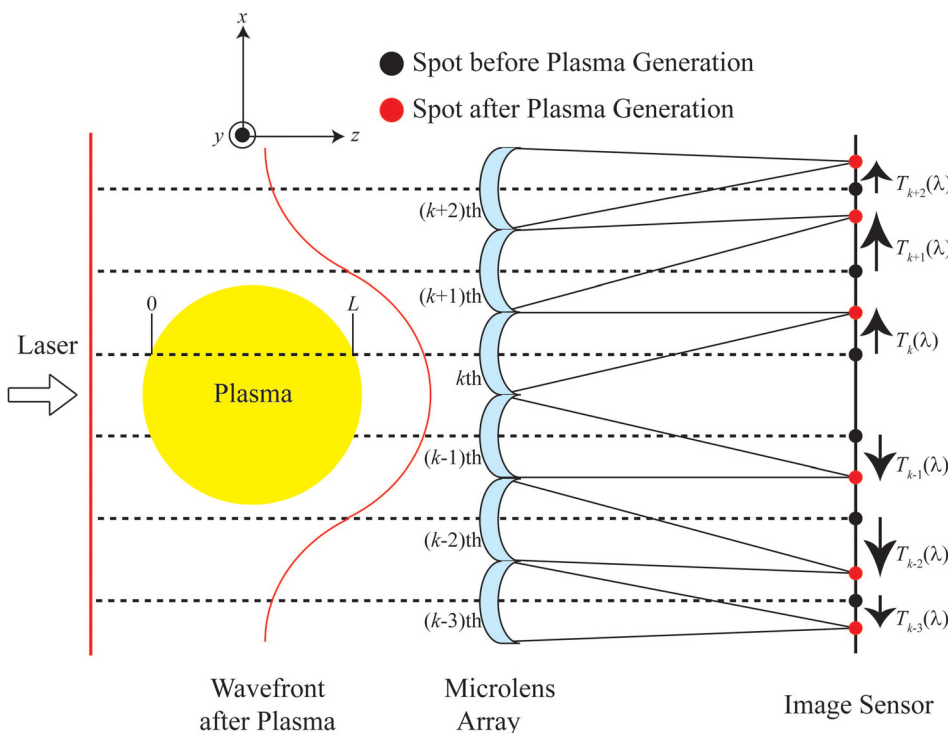

FIG. 4. Scheme of Shack-Hartmann type laser wavefront sensor for measuring electron density in discharge plasma.

camera (Andor Co., Ltd DH734–18F-73; minimum shutter speed = 5 ns; pixel size = 13 μm × 13 μm; pixel number = 1024 × 1024). The minimum detectable limit of electron densities was ~10^{23} m^{-3} for the microlens arrays with the focal length of 1 mm, ~10^{22} m^{-3} for 20 mm, and ~10^{20} m^{-3} for 467 mm.

The spatial resolution of the sensor is equal to the pitch among microlens P. On the other hand, a temporal resolution of the sensing system is determined by the shutter speed of the ICCD camera. Unless stated otherwise, the shutter speed of the ICCD camera was set to 50 ns in the electron density measurements. The repetitive gating operation of the ICCD camera requires a time interval of more than 2 s; thus, electron density measurements were carried out on a shot-to-shot basis changing the time delay of the ICCD trigger signal for each recording.

C. Fast framing video camera

The flare behavior was observed by using a fast framing video camera (Specialised Imaging Ltd. SIM; pixel size = 6.45 μm × 6.45 μm; pixel number = 1360 × 1024; minimum exposure time = 5 ns; detectable wavelength range = 358–890 nm) incorporating four ICCD cameras, whose operation timings can be determined separately. The shutter speed of each ICCD camera was set to 5 ns in $0 \leq t \leq 250$, and 20 ns in $300 \leq t \leq 550$ ns. In the preliminary experiment, we simultaneously recorded the voltage waveforms and the monitor out signals of the framing camera so many times, and identified the explosion timing on the voltage waveforms within the accuracy of ±10 ns. The accuracy of ±10 ns could not have a large influence on the temporal flare behavior evolving in the time scale of ~100 ns.

D. Spectrometer

Optical emission spectroscopy was conducted by using a combination of the ICCD camera (Andor Co., Ltd DH734-18F-73; minimum shutter speed = 5 ns; pixel size = 13 μm × 13 μm; pixel number = 1024 × 1024) and a motorized Czerny-Turner spectrograph (Andor Co., Ltd Shamrock 303i; focal length = 303 mm; inverse line dispersion = 9.64 nm/mm for 300 G/mm; wavelength resolution = 0.43 nm; simultaneously recorded spectrum range = 9.64 nm/mm × 13 μm × 1024 pixel = 128 nm for 300 G/mm). The input slit axis of the spectrometer was adjusted onto the center line along the axial direction of the electrodes, which is indicated in Fig. 2. The optical emission spectroscopy was carried out under exposure time of 50 ns and a single-shot scanning range of 430–570 nm.

III. RESULTS AND DISCUSSION

A. High speed photography

Figures 5(a)–5(l) show a typical spatiotemporal evolution of the plasma flares observed by using the fast framing video camera. The spatial reproducibility of the flare propagation lengths is represented in Figs. 5(c)–5(h) by the error ranges of ±150 μm. The light intensity increases from blue to red regions. The pseudocolor scales of each recording timing were

corrected based on the camera sensitivity and shutter speed. Therefore, it is allowed to compare the emitted light intensity among the different-timing shots. Prior to the appearance of the plasma flares, an electrical current starts to flow in $t < 0$ ns due to electric field emission from cathode protrusions.[24] When the current density exceeds a critical value, the explosive rupture of the cathode protrusions occurs, as observed at $t = 0$ ns in Fig. 5.

Figure 5(b) shows that the plasma flare was initiated on the anode at $t = 50$ ns. The anode flare is caused by the excessive anode heating due to the impact of high energy electrons emitted from a cathode surface and accelerated by a strong electric field in the vacuum gap.[24] The intense anode heating causes an explosive ejection of metallic anode vapor with a temperature of ~1 eV.[25] Subsequently, a fraction of the evaporated anode metal condensates into metallic solid, and the condensation energy is released to the remaining metallic anode vapor. The release of the condensation energy raises the temperature of the remaining metallic anode vapor to ~3 eV.[26] The metallic anode vapor is ionized by the collision with the high energy electrons emitted from the cathode, and as a consequence, a plasma flare is established on the anode.

Figures 5(c)–5(f) show that the plasma flare propagated from the anode to the gap center with a constant expanding speed of 6×10^3 m/s, which agreed well with other experimental results for copper anodes.[12,13] Here, we estimate the gas temperature of the anode flare T_g (eV) from its expanding speed. As a first-order approximation, it is supposed that the anode flare in $100 \leq t \leq 250$ ns was fully-ionized single fluid and propagated adiabatically into vacuum following the gaseous sphere expansion. The expansion speed of the anode flare v_{AF} (m/s) can be given by[26]

$$v_{AF} = \sqrt{\frac{4\omega\gamma}{\gamma - 1}}, \tag{1}$$

where ω (J/kg) is the internal energy of anode flare and γ is an adiabatic exponent. Since the copper ions are heavier than electrons by five orders of magnitude, the expansion speed is predominated by copper ion behavior. Therefore, the kinetic energy of the copper ions were considered for ω. The internal energy of the anode flare is described by

$$\omega \, (\text{J/kg}) = 11\,600 \, (\text{K/eV})$$
$$\times \frac{3}{2} \frac{N_A \, (1/\text{mol})}{M_{Cu} \, (\text{kg/mol})} k_B \, (\text{J/K}) T_g \, (\text{eV}), \tag{2}$$

where 11 600 (K/eV) is a conversion factor between energy and temperature, N_A (1/mol) is Avogadro's constant, M_{Cu} (kg/mol) is the atomic weight of copper ions, and k_B (J/K) is Boltzmann's constant. The use of Eqs. (1) and (2) provides the gas temperature of the anode flare T_g as follows:

$$T_g = \frac{v_{AF}^2 M_{Cu}(\gamma - 1)}{11\,600 \times 6 N_A \gamma k_B}. \tag{3}$$

Substituting the experimental result of $v_{AF} = 6 \times 10^3$ m/s and the monatomic gas exponent of $\gamma = \frac{5}{3}$ into Eq. (3), the gas
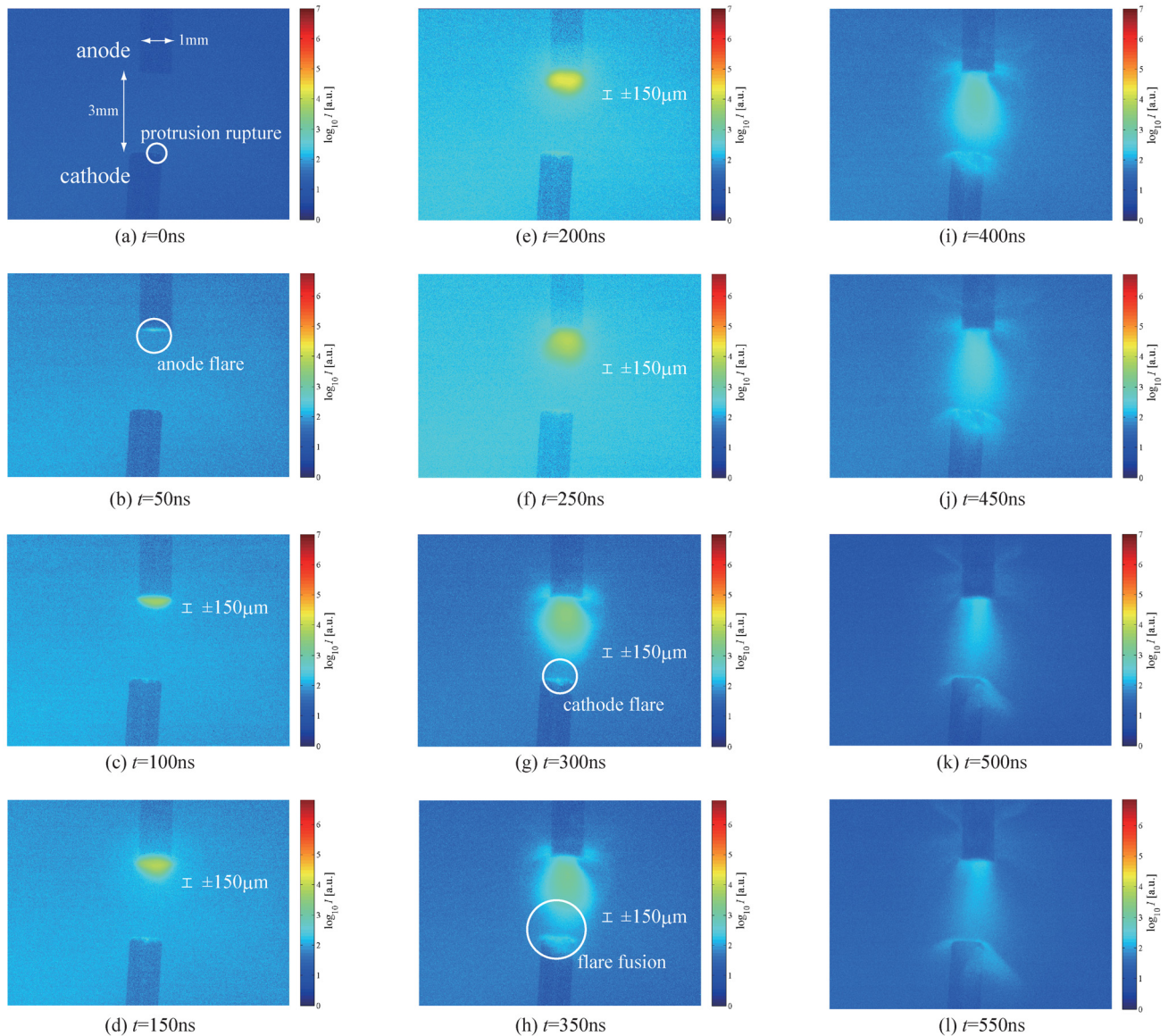
FIG. 5. Spatiotemporal evolution of plasma flare at $t =$ (a) 0, (b) 50, (c) 100, (d) 150, (e) 200, (f) 250, (g) 300, (h) 350, (i) 400, (j) 450, (k) 500, and (l) 550 ns, observed by using fast framing video camera. Error range of $\pm 150\,\mu$m represented in (c)–(h) shows spatial reproducibility of flare propagation length.

temperature of the anode flare is determined as $T_g \simeq 2$ eV in $100 \leq t \leq 250$ ns.

At $t = 300$ ns, a plasma flare was also initiated on the cathode surface, as shown in Fig. 5(g). Figure 5(h) shows that the anode flare encountered the cathode flare above the cathode surface at $t = 350$ ns, and a plasma channel was established over the interelectrode gap. After $t = 300$ ns, the anode flare no longer demonstrated the sphere expansion observed before $t = 250$ ns. The anode flare after $t = 300$ ns was seen to propagate in the y-axis preferably. Such unidirectional anode flare expansion along the y-axis suggests that the flare propagation was driven in the direction of the electric field over the interelectrode gap. After the establishment of the plasma channel, the plasma flares collapsed from $t = 400$ to 550 ns.

B. Optical emission spectroscopy

The optical emission spectroscopy was carried out by using the spectrometer for plasma composition analysis.

Figures 6(a)–6(d) show representative light emission spectra at $t = 200$, 300, 400, and 550 ns, respectively. The camera sensitivity and pseudocolor scales of each recording timing were all common, so that the emission intensity can be compared among the different-timing shots. At $t = 200$ ns, continuum radiation was predominant. Continuum radiation generally originates from four mechanisms: recombination, bremsstrahlung, electron attachment, and electron-neutral collisions. The recombination and bremsstrahlung are caused by the interactions between electrons and ions, while the other two processes arise from those between electrons and neutrals. In this study, the recombination and bremsstrahlung could be the cause of the continuum radiation because the neutral copper atom density was smaller than the ion density by 3 orders, as mentioned later. On the other hand, strong local peaks were not observed at 510.55, 515.32, and 521.82 nm, which are major line spectra of neutral copper atom Cu(I).[27] Therefore, little neutral copper atoms were
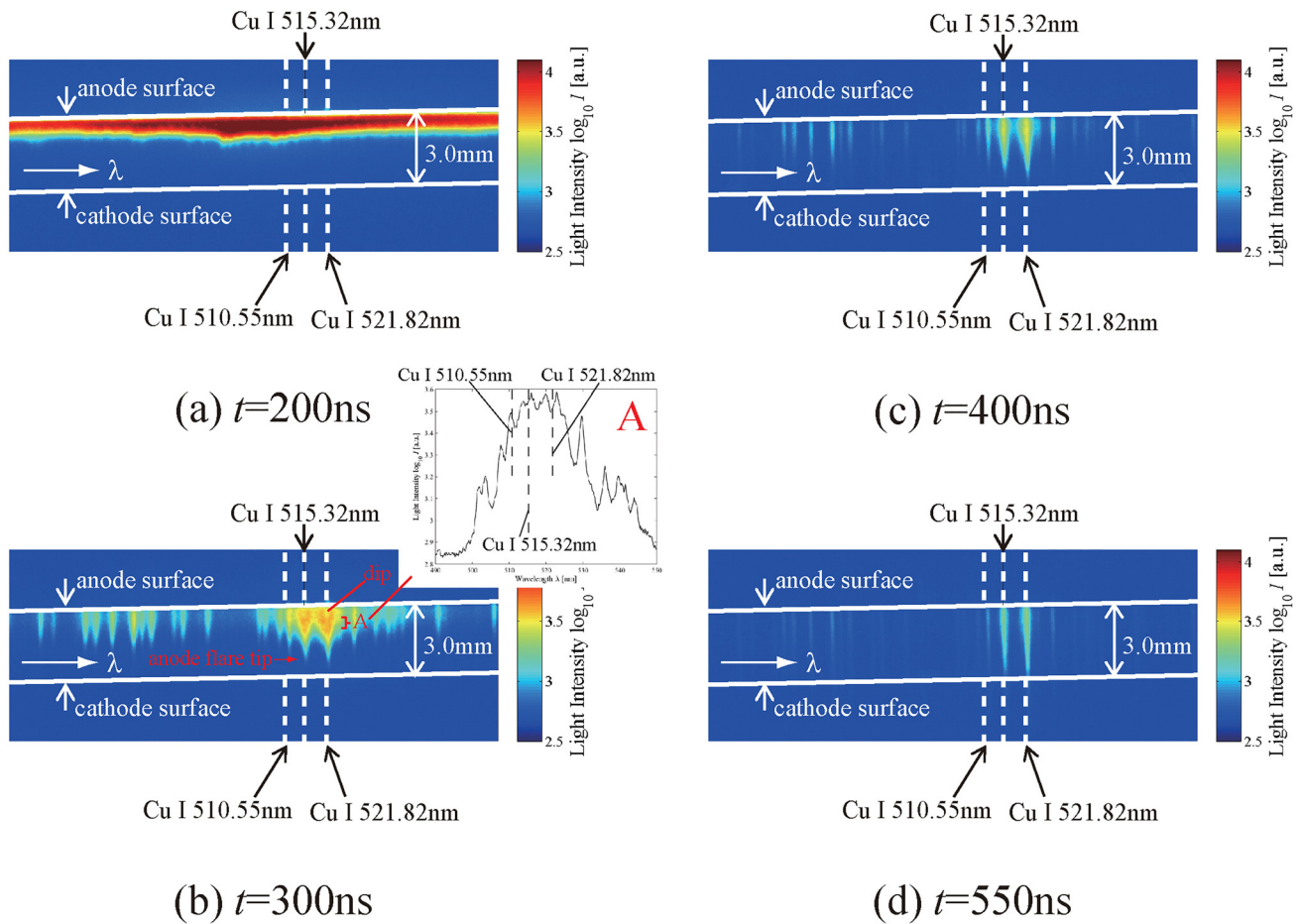
FIG. 6. Optical emission spectroscopy at $t =$ (a) 200, (b) 300, (c) 400, and (d) 550 ns conducted under temporal resolution of 50 ns.

included in the plasma flares at $t = 200$ ns. The plasma flares were almost fully ionized in the time range of $100 \leq t \leq 250$ ns. Such a small amount of neutral copper atoms in $100 \leq t \leq 250$ ns could be consistent with $T_g \simeq 2$ eV discussed in Subsection III A, because the composition of a copper vapor plasma under local thermodynamic equilibrium (LTE) demonstrates that the number density of neutral copper atoms is smaller than that of copper ions by a magnitude of 3 orders at $T_g \simeq 2$ eV.[28] Under the LTE condition, dominant copper ions at $T_g \simeq 2$ eV are Cu(III).[28] Since the translational temperature of Cu(III) reaches that of electrons within ~ 1 ns[29] and the energy relaxation time of ~ 1 ns was comparable to the propagation timescale of the anode flares, LTE could not be fully satisfied. The description on LTE in this paper is only for qualitative discussion.

The line spectra of neutral copper atoms Cu(I) were observed at $t = 300$ ns, as shown in Fig. 6(b). It should be noted that the Cu(I) line spectra were dominant only around the tip of the anode flare. On the other hand, in the region indicated by "A," the predominant radiation component was still continuum as shown in the accompanying spectrum of Fig. 6(b). According to the composition of a copper vapor plasma in LTE,[28] such stronger Cu(I) line spectra around the tip of the anode flare suggested a smaller ionization degree, resulting in lower T_g compared with region A. A possible mechanism of the spectral transition from the continuum to Cu(I) line components at the anode flare tips will be discussed in

Subsection III C. One more thing to note is that in the vicinity of the anode surface, there existed a spectral intensity dip at 521.82 nm. Such a spectral dip at the major Cu(I) line means radiation trap caused by the existence of neutral copper atoms. Therefore, it is suggested that the ionization degree and T_g in the vicinity of the anode surface were also lower than those in region A.

As mentioned in Subsection III A, the plasma channels were established at $t = 350$ ns. After the establishment of the plasma channels, the plasma flares were decomposed from $t = 400$ to 550 ns. At $t = 400$ and 550 ns, continuum radiation components disappeared and the Cu(I) line spectra were predominant over the interelectrode gap, as shown in Figs. 6(c) and 6(d). In the process of the flare decomposition, the radiation intensity at 510.55, 515.32, and 521.82 nm decreased with increasing time t. Such a decrease in the line spectral intensity corresponded to the decrease in the number density of neutral copper atoms.

C. Electron density imaging

Figures 7(a)–7(h) show a typical spatiotemporal evolution of two-dimensional electron density images of the plasma flares observed using the Shack-Hartmann sensor(s). The shot-to-shot variation of the absolute values of the electron densities was within $\pm 30\%$. Figures 7(a)–7(d) show that the plasma flares with high electron densities of 10^{24-25} m^{-3} propagated from
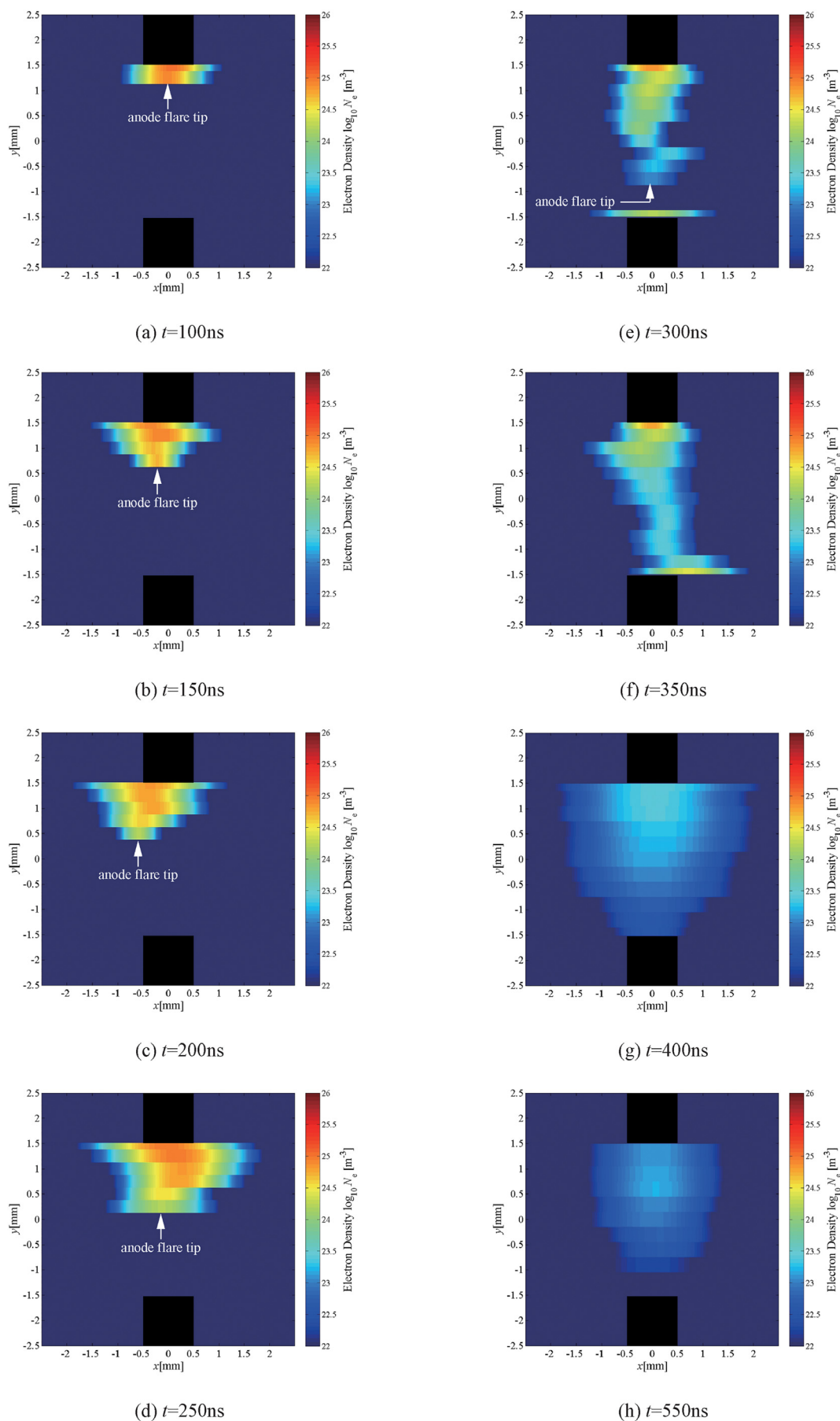
FIG. 7. Two-dimensional electron density distribution at $t =$ (a) 100, (b) 150, (c) 200, (d) 250, (e) 300, (f) 350, (g) 400, and (h) 550 ns. Shot-to-shot variation of electron density was within $\pm 30\%$.

the anode to the gap center with the expanding speed of 5–10×10^3 m/s. The flare propagation speed was in excellent agreement with 6×10^3 m/s, which was observed by the high-speed framing photography in $100 \leq t \leq 250$ ns. Since dominant valence number of ions was 2 in $100 \leq t \leq 250$ ns under the LTE condition, the pressure of the anode flares P_A (Pa) was 4–40×10^5 Pa, which was calculated by using $P_A = 11\,600(N_e + N_i)k_B T_g = 11\,600(N_e + \frac{N_e}{2})k_B T_g$, where N_i (m^{-3}) is the ion density. In that time range, the copper atom density was expected to be 10^{21-22} m^{-3} from the LTE composition.[28]

According to the spectroscopic measurement at $t = 200$ and 300 ns, the Cu(I) line intensity at the anode flare tips increased with increasing time. This suggested that the ionization degree and T_g at the anode flare tips decreased with increasing time. Since T_g in $100 \leq t \leq 250$ ns was almost 2 eV, that in $250 \leq t \leq 300$ ns could be below 2 eV. Here, the LTE condition is assumed in $250 \leq t \leq 300$ ns. Under LTE, electron temperature T_{el} (eV) is almost equal to T_g, and it could be also lower than 2 eV in $250 \leq t \leq 300$ ns. In the temperate range of $T_{el} \sim T_g < 2$ eV, the majority of ionic valence number Z is 1.[28]

Figure 8 shows the temporal evolution of the electron densities at the anode flare tips. Some examples of the anode flare tips are indicated in Figs. 7(a)–7(e). The error ranges in Fig. 8 represent the shot-to-shot variation in the electron densities at the anode flare tips. The data plots in Fig. 8 show the electron densities averaged over the several shots. From $t = 250$ to 300 ns, the electron densities at the anode flare tips showed a drastic decrease from 2.0×10^{24} to 2.8×10^{23} m^{-3}. Such an electron density reduction in the short time range of 50 ns is considered to be caused by a rapid electron consumption in the three-body recombination reaction:[30] $e + e + Cu(II) \rightarrow e + Cu(I)$. In the following, it is examined whether the rapid electron consumption was caused by the three-body recombination.

In the process of the electron density reduction, the reactions listed in Table I were taken into account. Considering $Z \simeq 1$ in $250 \leq t \leq 300$ ns, the three-body recombination caused by multivalent ions could not occur predominantly. In addition to the three-body recombination, electron

TABLE I. Reaction and rate coefficient.

Reaction	Rate coefficient
Electron ionization $e + Cu(I) \rightarrow e + e + Cu(II)$	$k_{el} = 1 \times 10^{-15}$ m^3/s (Ref. 31)
Three-body recombination $e + e + Cu(II) \rightarrow e + Cu(I)$	$k_{3b} = \frac{8.75 \times 10^{-39}}{T_{el}^{4.5}}$ m^6/s (Ref. 30)

impact ionization occurred simultaneously: $e + Cu(I) \rightarrow e + e + Cu(II)$.

The values of rate coefficients and related references are also indicated in Table I. The rate coefficient of the electron impact ionization k_{el} (m^3/s) is reported to be 1×10^{-15} m^3/s.[31] The three-body recombination rate k_{3b} (m^6/s) is described by $k_{3b} = (8.75 \times 10^{-39}) \times \frac{Z^3}{T_{el}^{4.5}}$.[30] In the parametric assessment above, T_{el} ($\simeq T_g$) was treated as an adjustable parameter and it was varied between, e.g., $1 \leq T_{el} \leq 1.5$ eV. The radiative recombination was not taken into account in the present analysis because its contribution[32] was negligibly small compared with the three-body recombination under an electron density of $N_e \sim 10^{24}$ m^{-3} and $T_{el} \sim 1$ eV, which were typical values for the anode flares in $250 \leq t \leq 300$ ns.

By using the parameters mentioned above, the following rate equations were solved simultaneously:

$$N_e = N_{Cu(II)}, \qquad (4)$$

$$\frac{dN_{Cu(I)}}{dt} = -k_{el}N_e N_{Cu(I)} + k_{3b}N_e^2 N_{Cu(II)}, \qquad (5)$$

$$\frac{dN_{Cu(II)}}{dt} = k_{el}N_e N_{Cu(I)} - k_{3b}N_e^2 N_{Cu(II)}. \qquad (6)$$

Here, $N_{Cu(I)}$ and $N_{Cu(II)}$ (m^{-3}) are number densities of Cu(I) and Cu(II), respectively.

Figure 9 shows the simulated temporal evolution of the electron and copper vapor densities at the anode flare tips. The solid curves show the simulated results for $T_{el} = 1.25$ eV. The error bars accompanying the solid curves indicate the
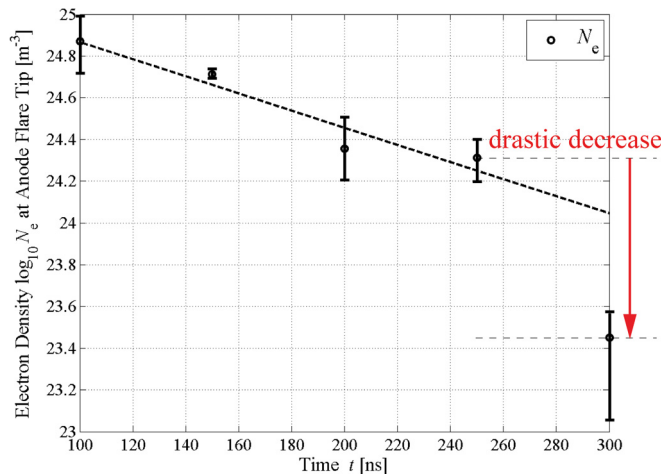
FIG. 8. Temporal evolution of electron density at anode flare tip. Data plot shows electron density averaged over several shot and error range represents shot-to-shot variation.
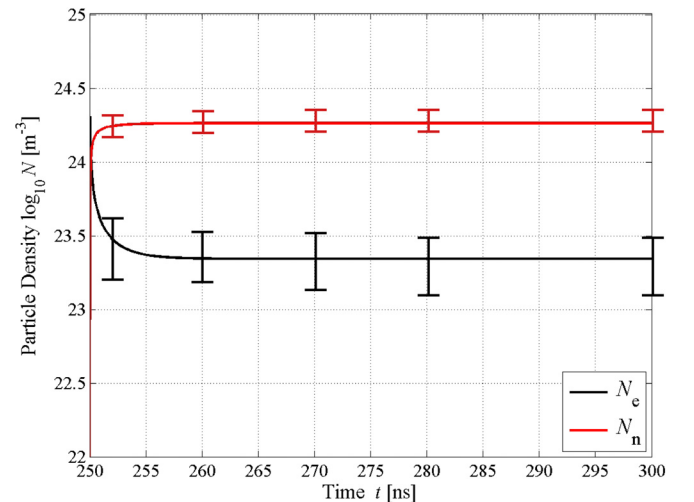
FIG. 9. Simulated temporal evolution of electron and copper vapor density at anode flare tip. Solid curve shows simulated result for $T_{el} = 1.25$ eV. Error bar indicates variation range of simulation result for $1 \leq T_{el} \leq 1.5$ eV. At $t = 250$ ns, the N_e was initialized at 2.0×10^{24} m^{-3} from present electron density measurement. The $N_{Cu(I)}$ was initialized at 1.0×10^{22} m^{-3}, which was determined by LTE composition of Cu vapor plasma in temperature of 1–1.5 eV.[28]

variation of the simulation results for the temperature range of $1 \leq T_{el} \leq 1.5$ eV. In the analytical simulation, we had to fix the electron density N_e and the Cu(I) density $N_{Cu(I)}$ at $t = 250$ ns as initial values. At $t = 250$ ns, the N_e was set to 2.0×10^{24} m^{-3} from the present electron density measurement. The simulation result was much influenced by the initial N_e. The $N_{Cu(I)}$ was initialized at 1.0×10^{22} m^{-3}, which was determined by the LTE composition of Cu vapor plasma in the temperature of 1–1.5 eV.[28] The simulation result was little affected by the initial $N_{Cu(I)}$. The calculated electron densities at the anode flare tips certainly decreased by one order of magnitude during several tens of ns, which agreed well with the drastic decrease in Fig. 8. Therefore, the significant electron density reduction observed in $250 \leq t \leq 300$ ns was qualitatively explained by the three-body recombination reaction. The three-body recombination makes a contribution to not only electron consumption but also neutral copper vapor production, as shown in Fig. 9. Therefore, the dominant spectral component at the anode flare tips transited from the continuum to Cu(I) line spectra in $250 \leq t \leq 300$ ns.

The number density of neutral copper atoms showed a decrease in $400 \leq t \leq 550$ ns, as mentioned in Subsection III B. In synchronization with the copper atom density reduction, the electron density also decreased with increasing time at the flare decomposition process. The electron density at $t = 550$ ns was 10^{21-22} m^{-3}, which was comparable to that in vacuum arc phases.[19] This means that the copper-vapor-contaminating conductive plasmas were gradually deconstructed and the vacuum arc discharges started to be established in a time range of $400 \leq t \leq 550$ ns.

IV. CONCLUSION

The plasma flares with high electron densities of 10^{25} m^{-3}, gas temperature of 2 eV, and pressure of 40×10^5 Pa were initiated on the anode and expanded to the vacuum gap with a propagation speed of 6×10^3 m/s in $100 \leq t \leq 250$ ns. The continuum spectral component was dominant in the high-electron-density anode flares. On the other hand, the dominant spectral component at the anode flare tips transited from the continuum to Cu(I) line spectra in $250 \leq t \leq 300$ ns due to the three-body recombination reaction, which also caused a significant decrease in the electron densities from 10^{24} to 10^{23} m^{-3} in the anode flare tips. The anode flare tips combined with the cathode plasma flares and the conductive plasma channels were established at $t = 350$ ns. The measurement of the Cu(I) line spectra showed that copper vapor densities decreased at the flare decomposition stage in $400 \leq t \leq 550$ ns, which meant that the plasma flares started to transform into the vacuum arc discharges.

ACKNOWLEDGMENTS

[1]H. C. Miller and G. A. Farrall, J. Appl. Phys. **36**, 1338 (1965).

[2]J. Ballat, D. König, and U. Reininghaus, IEEE Trans. Electr. Insul. **28**, 621 (1993).

[3]H. Kojima, T. Takahashi, N. Hayakawa, K. Hasegawa, H. Saito, and M. Sakaki, IEEE Trans. Dielectr. Electr. Insul. **23**, 3224 (2016).

[4]H. Kojima, T. Takahashi, M. Noda, K. Hasegawa, M. Sakaki, and N. Hayakawa, in *XXVII International Symposium on Discharges and Electrical Insulation in Vacuum* (2016), pp. 9–12.

[5]E. R. Kieft, J. J. A. M. Mullen, G. M. W. Kroesen, V. Banine, and K. N. Koshelev, Phys. Rev. E **70**, 056413 (2004).

[6]E. R. Kieft, J. J. A. M. Mullen, G. M. W. Kroesen, V. Banine, and K. N. Koshelev, Phys. Rev. E **70**, 066402 (2004).

[7]E. R. Kieft, J. J. A. M. Mullen, G. M. W. Kroesen, V. Banine, and K. N. Koshelev, Phys. Rev. E **71**, 026409 (2005).

[8]E. R. Kieft, K. Garloff, J. J. A. M. Mullen, and V. Banine, Phys. Rev. E **71**, 036402 (2005).

[9]E. R. Kieft, J. J. A. M. Mullen, and V. Banine, Phys. Rev. E **72**, 026415 (2005).

[10]J. A. Chiles, Jr., J. Appl. Phys. **8**, 622 (1937).

[11]S. P. Bugaev, A. M. Iskol'dskii, G. A. Mesyats, and D. I. Proskurovskii, Sov. Phys. Tech. Phys. **12**, 1625 (1968).

[12]R. B. Baksht, V. A. Kokshenev, and V. I. Manylov, Sov. Phys. Tech. Phys. **20**, 1069 (1976).

[13]I. D. Chalmers and B. D. Phukan, J. Phys. D: Appl. Phys. **12**, 1285 (1979).

[14]R. B. Baksht and V. I. Manylov, Sov. Phys. J. **14**, 1297 (1971).

[15]A. Anders, S. Anders, B. Jüttner, W. Bötticher, H. Löck, and G. Söhroder, IEEE Trans. Plasma Sci. **20**, 466 (1992).

[16]S. P. Bugaev, R. B. Baksht, E. A. Litvinov, and V. P. Stas'ev, High Temp. **14**, 1027 (1976).

[17]Y. Inada, T. Kamiya, S. Matsuoka, A. Kumada, H. Ikeda, and K. Hidaka, J. Instrum. **10**, C12007 (2015).

[18]Y. Inada, T. Kamiya, S. Matsuoka, A. Kumada, H. Ikeda, and K. Hidaka, IEEE Trans. Plasma Sci. **45**, 129 (2017).

[19]Y. Inada, S. Matsuoka, A. Kumada, H. Ikeda, and K. Hidaka, J. Appl. Phys. **121**, 103304 (2017).

[20]Y. Inada, S. Matsuoka, A. Kumada, H. Ikeda, and K. Hidaka, J. Phys. D: Appl. Phys. **45**, 435202 (2012).

[21]B. Platt and R. V. Schack, Opt. Sci. Cent. Newsl. **5**, 15 (1971).

[22]D. Malacara, *Optical Shop Testing* (Wiley-Interscience, New York, 1978), Chap. 10.

[23]R. L. Boxman, J. Appl. Phys. **45**, 4835 (1974).

[24]P. G. Slade, *The Vacuum Interrupter: Theory, Design, and Application* (CRC Press, Boca Raton, 2007), Chap. 1, pp. 121–176.

[25]S. I. Anisimov, A. M. Bonch-Bruevich, M. A. Elfyashevich, Y. A. Imas, N. A. Pavlenko, and G. S. Romanov, Sov. Phys. Tech. Phys. **11**, 945 (1967).

[26]R. B. Baksht, N. A. Ratakhin, and B. A. Kablambaev, Sov. Phys. Tech. Phys. **27**, 1091 (1982).

[27]National Institute of Standards and Technology (NIST), http://physics.nist.gov/ for NIST atomic spectra database.

[28]M. B. P. Kloc, V. Aubrecht, and O. Coufal, J. Phys. D: Appl. Phys. **48**, 055208 (2015).

[29]L. Spitzer, *Physics of Fully Ionized Gases*, 2nd Rev. ed. (Interscience Publishers, New York, 1962), Chap. 5.3, pp. 131–136.

[30]A. V. Gurevich and L. P. Pitaevskii, Sov. Phys. JETP **19**, 870 (1964).

[31]P. Teulet, J. J. Gonzalez, A. Mercado-Cabrera, Y. Cressault, and A. Gleizes, J. Phys. D: Appl. Phys. **42**, 175201 (2009).

[32]H. A. Kramers, Philos. Mag. **46**, 836 (1923).